Article

Transdimensional anomalous Hall effect in rhombohedral thin graphite

https://doi.org/10.1038/s41586-026-10471-1

Received: 11 April 2025

Accepted: 31 March 2026

Published online: 29 April 2026

Check for updates

Qingxin Li[1,17], Hua Fan[2,3,17], Min Li[4,17], Yinghai Xu[1], Junwei Song[1], Anqi Wang[5], Kenji Watanabe[6], Takashi Taniguchi[7], Jing-Jing Chen[8], Zhenbing Tan[8], Jie Shen[5], Hua Jiang[9], James C. Hone[10], Cory R. Dean[11], Kostya S. Novoselov[12], Xin-Cheng Xie[9,13], Geliang Yu[1,14] ✉, Yue Zhao[2] ✉, Jianpeng Liu[4,15] ✉ & Lei Wang[1,14,16] ✉

Anomalous Hall effect (AHE), occurring in materials with broken time-reversal symmetry, epitomizes the interplay between magnetic order and electron orbital motions[1–4]. In two-dimensional (2D) systems, AHE is coupled with out-of-plane orbital magnetization associated with in-plane chiral orbital motions. In three-dimensional (3D) systems, in which sample thickness far exceeds a vertical coherence-transport length l_z, the AHE is effectively a thickness-averaged 2D counterpart[4]—still governed by out-of-plane orbital magnetization arising from in-plane orbital motions. Here we report the experimental observation of a fundamentally new type of AHE that couples both in-plane and out-of-plane orbital magnetizations in multilayer rhombohedral graphene, shown by pronounced Hall resistance hysteresis under both in-plane and out-of-plane magnetic fields. This state emerges from a peculiar metallic phase that spontaneously breaks time-reversal, mirror and rotational symmetries driven by electron–electron interactions. By measuring multiple devices spanning 3–15 layers, we find that this phenomenon emerges only within an intermediate thickness of 2–5 nm. Theoretical calculations show that carriers within this window can sustain coherent orbital motions both within and across the 2D plane. Together, these identify an uncharted 'transdimensional' regime between 2D and 3D, in which the sample thickness is much larger than atomic spacing yet remains comparable to l_z, for the emergence of this new state of matter—transdimensional AHE. Our findings point to a distinct class of AHE, opening an unexplored model for correlated and topological physics in transdimensional landscapes.

Electrons travelling through a material under a magnetic field follow a curved trajectory because of the Lorentz force, generating a Hall voltage perpendicular to both the current flow and magnetic field directions[5]. Although the ordinary Hall effect requires an external magnetic field, the anomalous Hall effect (AHE) arises even without one, typically in ferromagnetic systems with broken time-reversal symmetry[4]. AHE can arise from extrinsic mechanisms such as skew scattering[6] and side jumps[7]. It can also originate from an intrinsic mechanism driven by momentum-space Berry curvature, which is fundamentally linked to the topological properties of conducting electrons[2–4]. In conventional magnetic systems, magnetization is usually contributed by both spin degrees of freedom and orbital magnetization. The latter results from the interaction between spin and the orbital motion of electrons by spin–orbit coupling (SOC), which is indispensable for the intrinsic AHE. This scenario applies to ferromagnetic metals[2,3] and ferromagnetic semiconductors[8], as well as magnetic topological materials[9–11]. Defying this SOC-driven scenario, twisted van der Waals systems have recently shown a different cause of AHE: it can emerge in a Coulomb-interaction-driven orbital ferromagnetic state, spontaneously breaking time-reversal symmetry devoid of SOC[12]. In these SOC-negligible systems, both integer and fractional quantum anomalous Hall effects (QAHEs) are observed[13–17]. Nevertheless, regardless of whether orbital magnetization stems from SOC or Coulomb interactions, all observed AHEs and QAHEs, at present, obey an

[1]National key Laboratory of Solid-State Microstructures, School of Physics, Nanjing University, Nanjing, China. [2]Department of Physics, State Key Laboratory of Quantum Functional Materials, Guangdong Basic Research Center of Excellence for Quantum Science, Southern University of Science and Technology (SUSTech), Shenzhen, China. [3]Guangdong Provincial Key Laboratory of Quantum Engineering and Quantum Materials Institute for Advanced Materials, South China Academy of Advanced Optoelectronics, South China Normal University, Guangzhou, China. [4]School of Physical Science and Technology, ShanghaiTech Laboratory for Topological Physics, ShanghaiTech University, Shanghai, China. [5]Beijing National Laboratory for Condensed Matter Physics, Institute of Physics, Chinese Academy of Sciences, Beijing, China. [6]Research Center for Electronic and Optical Materials, National Institute for Materials Science, Tsukuba, Japan. [7]Research Center for Materials Nanoarchitectonics, National Institute for Materials Science, Tsukuba, Japan. [8]International Quantum Academy, Shenzhen, China. [9]Interdisciplinary Center for Theoretical Physics and Information Sciences (ICTPIS), Fudan University, Shanghai, China. [10]Department of Mechanical Engineering, Columbia University, New York, NY, USA. [11]Department of Physics, Columbia University, New York, NY, USA. [12]Institute for Functional Intelligent Materials, National University of Singapore, Singapore, Singapore. [13]International Center for Quantum Materials, School of Physics, Peking University, Beijing, China. [14]Jiangsu Physical Science Research Center, Nanjing, China. [15]Liaoning Academy of Materials, Shenyang, China. [16]Shishan Laboratory, Suzhou Campus of Nanjing University, Suzhou, China. [17]These authors contributed equally: Qingxin Li, Hua Fan, Min Li. ✉e-mail: yugeliang@nju.edu.cn; zhaoy@sustech.edu.cn; liujp@shanghaitech.edu.cn; leiwang@nju.edu.cn

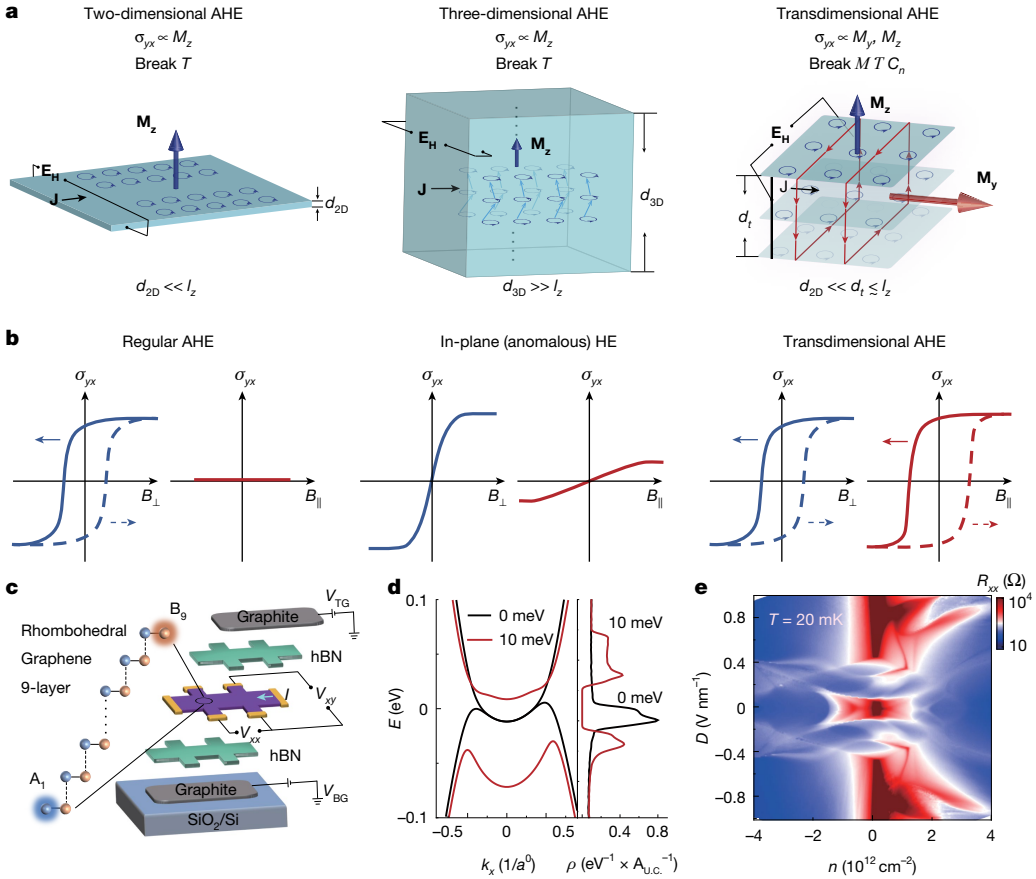


Fig. 1 | Dimensionality perspective of AHE and basic characterizations on rhombohedral ennealayer graphene. a, Illustration of the 2D AHE (left), 3D AHE (middle) and transdimensional AHE (right). The transdimensional AHE with broken $\mathcal{T}$, n-fold rotational C_n and vertical mirror $\mathcal{M}_y$ symmetries can host both out-of-plane magnetization and in-plane orbital magnetization. **b**, Illustration of the expected magnetic response of three different types of AHE. Regular AHE (left) with only out-of-plane magnetic hysteresis; in-plane Hall effect (middle) with linear Hall resistance driven by in-plane external magnetic field; transdimensional AHE (right) with both out-of-plane and in-plane magnetic hysteresis. **c**, Schematic of the dual-gated Hall-bar device. Left, atomic structure of rhombohedral ennealayer graphene, with highlighted orbitals located at the bottom (A_1) and top (B_9) layers of ennealayer graphene dominating the wavefunctions of the low-energy bands. **d**, Left, tight-binding calculations of the energy dispersion near the **K** point of rhombohedral-stacked ennealayer graphene under an electric potential $\Delta = 0$ meV (black) and $\Delta = 10$ meV (red). Right, the single-particle DOS, ρ, compared with energy under $\Delta = 0$ meV (black) and $\Delta = 10$ meV (red). **e**, Measured longitudinal resistance R_{xx} as a function of n and D at $T = 20$ mK, and $B = 0$ T. The corresponding ρ_{xy} map is shown in Extended Data Fig. 2d.

orthogonality rule: the directions of orbital magnetization **M**, current flow **J** and transverse electric field $\mathbf{E}_H$ associated with Hall voltage must be mutually perpendicular, that is, $\mathbf{M} \propto \mathbf{J} \times \mathbf{E}_H$.

Dimensionality effect on AHE

A distinct, yet long-overlooked, perspective to explain and classify AHE is the dimensionality in which it emerges. In two dimensions (Fig. 1a, left), AHE is characterized by chiral orbital motions within the plane and is coupled with out-of-plane orbital magnetization M_z (Fig. 1b, left). AHE driven by in-plane spin magnetization, parallel to current flow, has been theoretically proposed in the literature[18–20] (Fig. 1b, middle). These approaches require a specially designed form of SOC, which couples in-plane spin magnetization to out-of-plane orbital magnetization. Therefore, this scenario can still be classified as the AHE generated by out-of-plane orbital magnetization. In three dimensions (Fig. 1a, middle), carriers are allowed to tunnel and/or get scattered along the third spatial dimension with a coherent-transport length scale l_z. In these systems, the thickness of the sample d is much larger than l_z along the vertical direction. As a result, the coherent out-of-plane orbital motions of electrons would be overwhelmed by momentum-relaxing scattering and dephasing processes within the sample. Thus, the AHE of the 3D system would be manifested as its 2D counterpart averaged over the sample thickness, which can be considered as coupling with M_z, too. However, an unexplored regime is when d is much larger than the atomic layer thickness yet smaller than l_z (Fig. 1a,b, right). In this 'transdimensional' regime, carriers may undergo coherent orbital motions both within and out of the 2D plane. Under certain symmetry-broken conditions, this can give rise to a fundamentally new type of AHE that is coupled with both out-of-plane orbital magnetization M_z and in-plane orbital magnetization M_y, a component parallel to current flow **J**, which does not rigorously follow the $\mathbf{M} \propto \mathbf{J} \times \mathbf{E}_H$ orthogonality rule. This points towards an unprecedented type of AHE, which we term as transdimensional anomalous Hall effect (TDAHE).

Here we report the observation of a fundamentally new type of AHE in multilayer rhombohedral graphene that couples both out-of-plane and in-plane orbital magnetizations. From transport measurements across trilayer, pentalayer, heptalayer, ennealayer, decalayer, hendecalayer and pentadecalayer rhombohedral graphene devices, we find that this phenomenon emerges only within an intermediate thickness window (2–5 nm). These results are consistent with the transdimensional transport picture and experimentally identify this distinct transdimensional regime in the rhombohedral graphene system. The main text focuses on the ennealayer device, whereas devices with other thickness values are presented in Extended Data Fig. 8. Unlike thinner rhombohedral graphene structures that host only in-plane orbital motions and form conventional out-of-plane magnetization[21–24], our

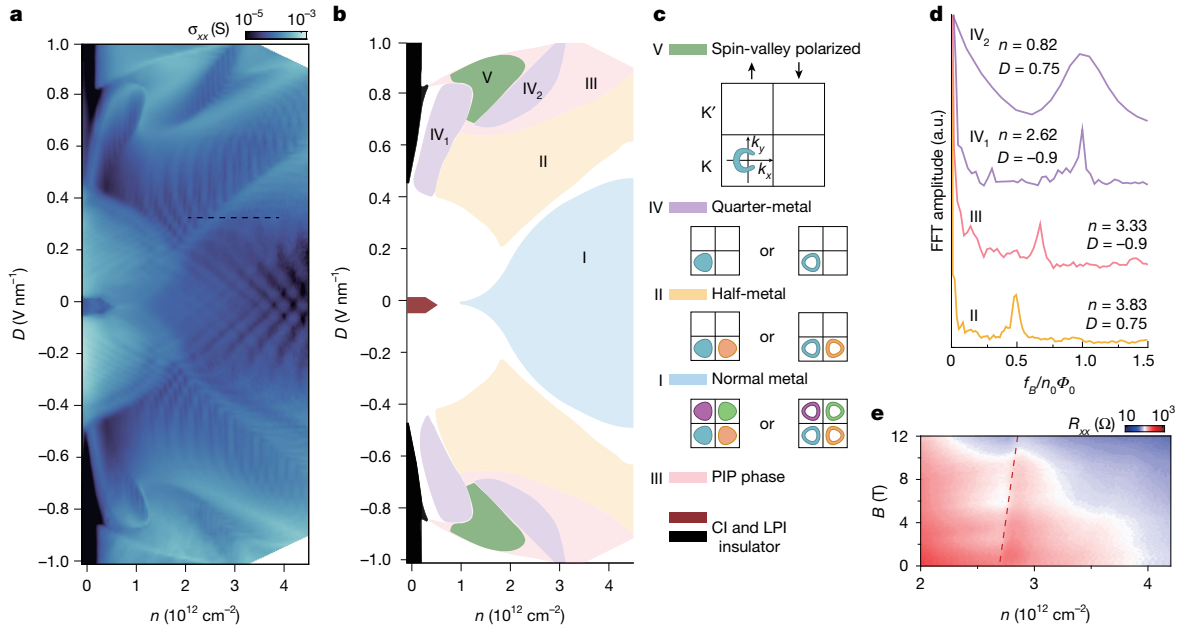


Fig. 2 | Phase diagram and fermiology in the conduction band. a, Map of the longitudinal conductivity σ_{xx} plotted against n and the displacement field D under a magnetic field $B_\perp = 4$ T and base temperature $T = 15$ mK. **b**, Schematic showing the main phases in **a**. The differently coloured regions, labelled with distinct Roman numerals, represent distinct spin- and valley-polarized flavours: I, normal metal; II, half-metal; III, partial isospin-polarized (PIP) metal; and IV, quarter-metal. Here, we find an unreported metallic phase (green region) in V. **c**, Illustration of various symmetry-broken metallic phases and the correlated insulator (CI), layer-polarized insulator (LPI) in **b**, along with schematically possible Fermi surface contours extracted on the basis of Fourier transforms. The filled colours in Fermi surface contours represent the spin and valley flavours. Phase V exhibits a new peculiar Fermi surface with a crescent shape (for more details, see Fig. 4d and the main text). **d**, Fast Fourier transformation (FFT) analysis of the quantum oscillations in quarter-metal, PIP and half-metal phases. The specified values of n and D are expressed in units of 10^{12} cm^{-2} and V nm^{-1}. Our range of magnetic field for taking FFT in phase IV_2 and II is about 0–6 T, and for phase IV_1 and III is about 0–5 T. **e**, Map of R_{xx} as a function of n and $B_\parallel$ at $D = 0.35$ V nm^{-1}. The data are taken along the horizontal black dashed line in **a**. The red dashed line corresponds to the boundary of the half-metal phase with spin-polarization and the normal metal phase without spin-polarization. a.u., arbitrary units.

nine-layer rhombohedral graphene possesses a d value falling providentially within the transdimensional range– much exceeding atomic layer thickness while smaller than l_z. In a spin-valley-polarized region near van Hove singularity (VHS), we detect robust TDAHE shown by pronounced Hall resistance hysteresis under both in-plane and out-of-plane external magnetic fields. Hartree–Fock calculations suggest that in the small doping and intermediate-D regime, electron–electron interactions induce spontaneous breaking of C_n rotational and $\mathcal{M}_y$ mirror symmetries, resulting in a Fermi surface with a crescent-shaped contour. This emergent asymmetric Fermi surface, combined with spontaneous time-reversal symmetry breaking, supports an in-plane magnetization parallel to the current flow for the first time, thereby endowing a fundamentally new type of AHE—TDAHE.

Phase diagram of rhombohedral ennealayer graphene

The structure of our nine-layer rhombohedral graphene device is shown in Fig. 1c. Low-energy sublattice sites localized in the outermost layers cause $E \propto \pm|k|^N$ energy dispersion, making the D-tuned DOS of nine-layer rhombohedral graphene very large (Fig. 1d). Figure 1e shows the longitudinal resistance R_{xx} compared with n and D at magnetic field $B = 0$ and $T = 15$ mK. At $n = 0$, we observe an insulating phase at high $|D|$ associated with the layer-polarized state and another insulator at $D = 0$, which defies the single-particle picture (Fig. 1d and Extended Data Fig. 2). Similar insulating behaviours near charge neutrality, including layer-polarized and interaction-driven insulating states, were reported in earlier transport studies on thick rhombohedral graphene[25–27].

Beyond the charge-neutral symmetry-breaking insulator, we also uncover spontaneously symmetry-broken metals in small-n and large-D regimes, in which D-enhanced VHSs lead to divergent density of states (DOS) for the emergence of strongly correlated electronic states. Figure 2a shows σ_{xx} compared with n and D at $B_\perp = 4$ T on the electron-doped side. A series of transitions (white regions) divides the metallic regime into distinct phases with different spin and valley polarizations[28–30] (Fig. 2b). Phase I corresponds to a normal metal with fourfold-degenerate Landau levels, whereas II and IV exhibit twofold and onefold degeneracies, respectively, identified by Fourier analysis (Fig. 2d), and are assigned to half-metal and quarter-metal states. In phase IV, strong exchange interactions stabilize a ferromagnetic ground state consistent with Stoner ferromagnetism[28–32], accompanied by out-of-plane magnetic hysteresis (Extended Data Fig. 3). Moreover, the evolution of phase II with the $B_\parallel$ (Fig. 2e) suggests a spin-polarized but valley-unpolarized phase stabilized by $B_\parallel$. Finally, phase III shows an oscillation frequency $0.5 < f_\nu < 1$ (Fig. 2d), corresponding to the partially isospin-polarized (PIP) phase in which the single Fermi surface simultaneously accommodates two majority and two minority isospin flavours.

Transdimensional anomalous Hall state

In these spontaneously symmetry-broken metallic phases, phase V exhibits a striking absence of quantum Shubnikov–de Haas (SdH) oscillations with increasing $B_\perp$, situated between two quarter-metal phases and a PIP phase in the $\sigma_{xx}(n, D)$ map (Fig. 3a). Phase V persists without Landau-level formation up to $B_\perp = 13$ T (Extended Data Fig. 4a–c), indicating a robust strongly correlated ground state that emerges from enhanced e–e correlations at low density and large D. Under strong $B_\perp$, this correlation-driven state prevails over quantum Hall states, suppressing conventional Landau-level features.

We then probe the magnetic character of phase V by $B_\parallel$ and $B_\perp$ field-dependent R_{xx} and R_{xy}. We observe hysteresis loops in both R_{xy} and R_{xx} with $B_\perp$, and unexpected pronounced hysteresis loops with $B_\parallel$, as shown in Fig. 3b–e. Artefacts from residual $B_\perp$ components causing

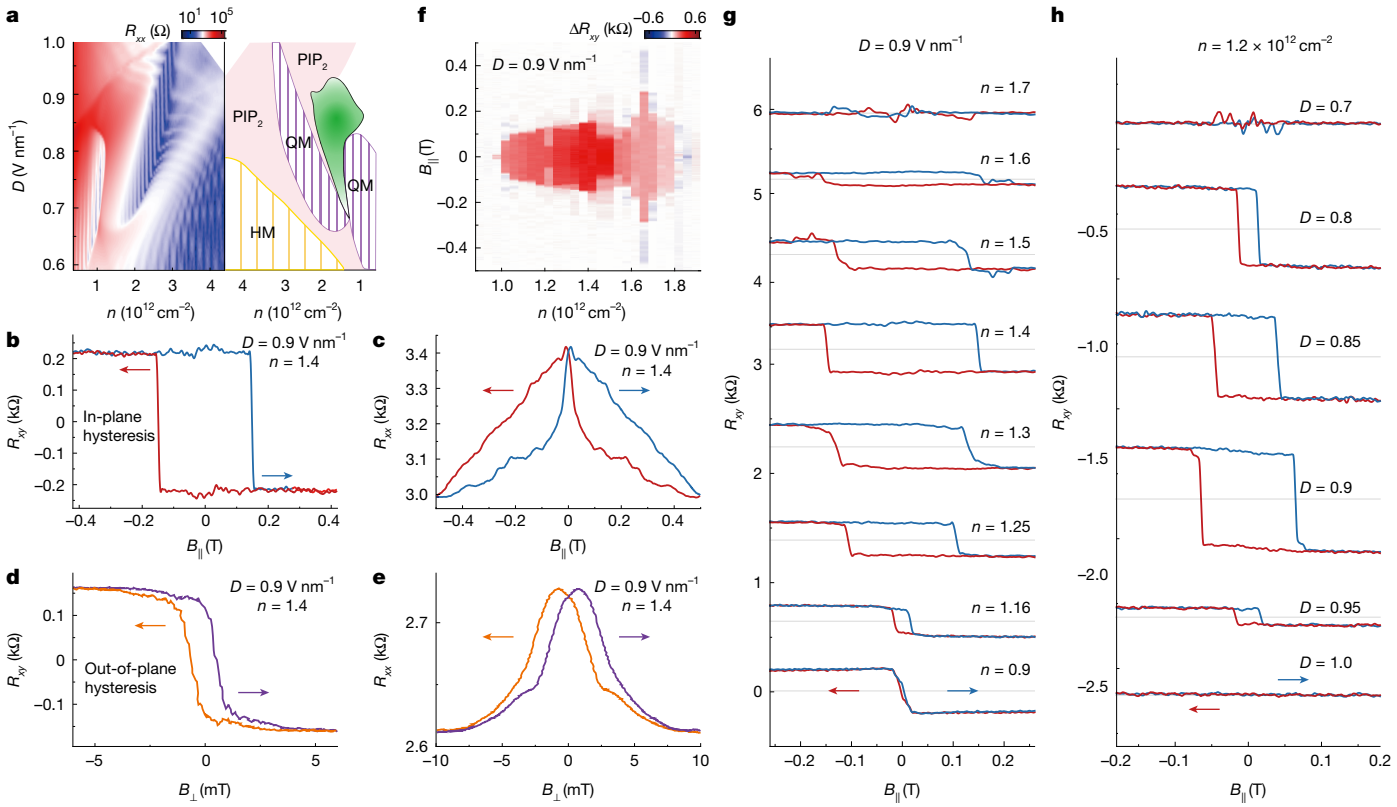


Fig. 3 | TDAHE with unique in-plane orbital magnetization and out-of-plane magnetization. a, Map of R_{xx} plotted against D and n at $B_\perp = 4$ T, for 0.6 V nm^{-1} ⩽ D ⩽ 1.0 V nm^{-1}. Illustration of different isospin flavours and TDAHE state (green region) are shown in the right panel. **b**,**c**, Anti-symmetrized Hall resistance R_{xy} (**b**) and symmetrized R_{xx} (**c**) measured as $B_\parallel$ is swept back and forth (marked by red and blue arrows) at $n = 1.4 \times 10^{12}$ cm^{-2} and $D = 0.9$ V nm^{-1}. For the coercive field, we can theoretically estimate it using $H_c \sim \Delta E/\mu_0 M_p$, where $\Delta E \sim 0.06$ meV per electron is the excitation energy between the lowest excited state and the ground state, and M_p is the in-plane orbital moment carried by each electron. A qualitative estimate gives a $H_c \sim 0.5$ T, consistent with experimental measurements. **d**,**e**, R_{xy} (**d**) and R_{xx} (**e**) measured as $B_\perp$ is swept back and forth (marked by orange and purple arrows) at $n = 1.4 \times 10^{12}$ cm^{-2} and $D = 0.9$ V nm^{-1}. Measurements in **b**–**e** are performed in two separate cooldowns with slightly different base temperatures (15 mK and 20 mK, respectively). **f**, Hall resistance difference ΔR_{xy} ($\Delta R_{xy} = R_{xy}^{B_\parallel\uparrow} - R_{xy}^{B_\parallel\downarrow}$) as a function of n and $B_\parallel$ at $D = 0.9$ V nm^{-1}. **g**, The parallel-magnetic-field dependence of R_{xy} at several selected carrier density n values (in units of 10^{12} cm^{-2}) at $D = 0.9$ V nm^{-1}, $T = 50$ mK. **h**, The parallel-magnetic-field dependence of R_{xy} at several selected displacement fields D values (in units of V nm^{-1}) at $n = 1.2 \times 10^{12}$ cm^{-2} and $T = 50$ mK.

the $B_\parallel$ hysteresis are rigorously ruled out (see Methods and Extended Data Figs. 5 and 7c). The $B_\perp$-induced R_{xy} hysteresis loop, beginning at approximately $B_\perp = \pm 3$ mT, shows a coercive field comparable to that observed in the quarter-metal phase (Extended Data Fig. 3). Thus, this hysteresis may originate from the Stoner-type isospin ferromagnetism. However, the coercive field of $B_\parallel$-induced R_{xy} hysteresis loop is about 160 mT (can reach as large as 500 mT under different n and D), which is significantly larger than the contribution from isospin orders. The unambiguous magnetic hysteresis loop observed indicates the presence of TDAHE with coexisting in-plane orbital magnetization and out-of-plane magnetization. Unlike the established model of exchange-interaction-driven Stoner ferromagnetism, the giant in-plane orbital ferromagnetism discovered here represents one of the first observations of its kind. We now turn to a detailed investigation of this AHE induced by in-plane orbital magnetization.

Doping and displacement field tuning

Figure 3h shows the D range for in-plane magnetization. With n fixed at 1.2×10^{12} cm^{-2}, accompanying the disappearance of the quarter-metal phase, the in-plane orbital magnetization emerges at $D = 0.7$ V nm^{-1}. As D increases, the magnitude of AHE initially enhances and then diminishes, exhibiting a maximum anomalous Hall signal at $D = 0.9$ V nm^{-1}, eventually vanishes at $D = 1.0$ V nm^{-1}, in which the PIP phase begins to develop. Theoretically, the in-plane magnetization also decays with the increase of displacement field after reaching some optimal value of D, following the same trend as the coercive field (Supplementary Information). Figure 3g shows a non-monotonic variation of the in-plane orbital magnetization with n at $D = 0.9$ V nm^{-1}. The $B_\parallel$-induced hysteresis loop appears at $n = 1 \times 10^{12}$ cm^{-2}, and maximizing at $n = 1.4 \times 10^{12}$ cm^{-2}. Beyond this point, the AHE signal gradually decreases and collapses at $n = 2 \times 10^{12}$ cm^{-2}, in which the quarter-metal phase develops. Notably, near the quarter-metal and TDAHE phase boundary, we observe an electric field hysteresis loop (Extended Data Fig. 6a–d). These hysteretic behaviours may signal a first-order phase transition separating two distinct Fermi surface topologies[29], indicative of competing ground states at the interface of quarter-metal and TDAHE.

Figure 3f maps the Hall resistance difference ΔR_{xy} between forward and backward B sweeps ($\Delta R_{xy} = R_{xy}^{B_\parallel\uparrow} - R_{xy}^{B_\parallel\downarrow}$) compared with n and $B_\parallel$ at $D = 0.9$ V nm^{-1}. This map captures the evolutionof the in-plane magnetization—emergence, strengthening and collapse—and a switching magnetic order behaviour occurring near the density at which the hysteresis loop almost vanishes (Extended Data Fig. 6e). Doping-induced switching magnetic order in Chern insulators has been reported previously in twisted and rhombohedral graphene multilayers systems[21,33,34], in which the magnetization changes sign within a phase with fixed valley polarization[35]. Unlike these switching behaviours in moiré Chern insulators driven by topological edge states[33,35], our moiré-free nine-layer rhombohedral graphene exhibits this reversal in a gapless metallic phase. The magnetization reversal here is more

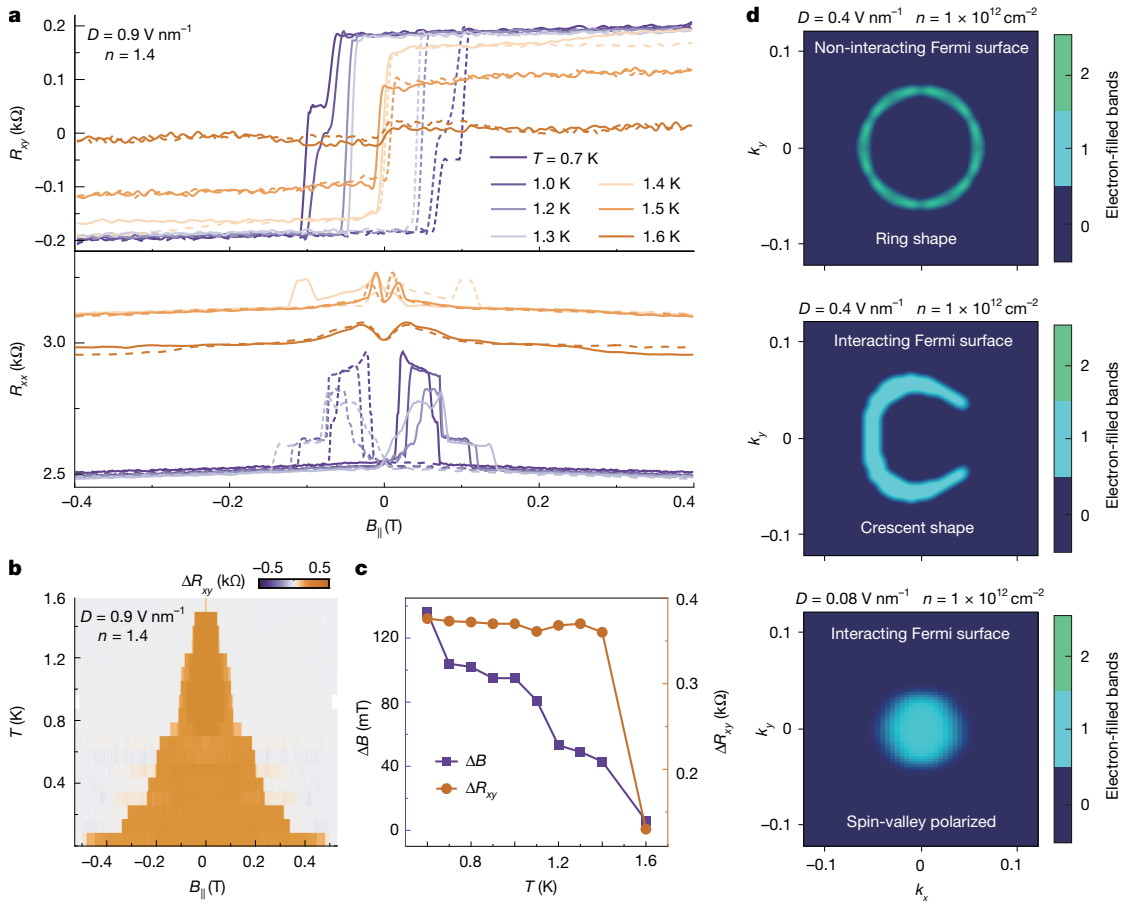


Fig. 4 | Temperature dependence of in-plane magnetic hysteresis and Hartree–Fock calculations. a, Magnetic field dependence of R_{xy} and R_{xx} at selected temperatures with a displacement field of $D = 0.9$ V nm^{-1} and a carrier density $n = 1.4 \times 10^{12}$ cm^{-2} in device B. **b**, Hall resistance difference ΔR_{xy} as a function of T and $B_{\parallel}$ at $n = 1.4 \times 10^{12}$ cm^{-2} and $D = 0.9$ V nm^{-1} in device B. The coercive field of $B_{\parallel}$-induced R_{xy} hysteresis loop can reach up to as large as 500 mT at 20 mK. The magnitude of the in-plane orbital ferromagnetism is suppressed with increasing temperature, evidenced by shrinking coercive field and lowering the ΔR_{xy}. **c**, Coercive field ΔB and ΔR_{xy} plotted as a function of T from the same data partially shown in **b**. The temperature-dependent data are taken from device B and the corresponding results from device A are shown in Extended Data Fig. 9d,e. **d**, Hartree–Fock calculations of Fermi contours. The different colours in the colour bar represent different numbers of isospins in the electron-filled energy bands. All plotted values are integer occupations; the apparent smoothing arises solely from Gaussian interpolation applied to the discrete Fermi surface data for visual clarity. The top panel plots the ring-shaped non-interacting Fermi surface of the system when a vertical electric field $D \gtrsim 0.3$ V nm^{-1}. The middle panel shows a peculiar metallic state with a crescent-shaped Fermi surface incorporating dominant long-range Coulomb electron–electron interactions, exhibiting complete spin and valley polarization. The bottom panel shows a regular interacting spin-valley polarized Fermi surface when electric field is small (or when n is large).

likely to arise from the density-dependent orbital magnetization of Bloch states with finite Berry curvature[34].

Temperature dependence

With n fixed at 1.4×10^{12} cm^{-2} and $D = 0.9$ V nm^{-1}, we examine temperature dependence of in-plane orbital magnetization. Figure 4a–c shows the temperature (T) dependence of $B_{\parallel}$-induced hysteresis loops and the map of ΔR_{xy} as a function of $B_{\parallel}$ and T. The magnitude of the in-plane orbital ferromagnetism is suppressed with increasing T, evidenced by shrinking coercive field and lowering the ΔR_{xy}. This ferromagnetism persists up to about $T_{c\parallel} = 1.6$ K. Although the coercive field decreases monotonically with T, the anomalous Hall signal remains nearly constant up to 1.5 K before dropping sharply (Fig. 4c).

This suppression may result from two possible mechanisms. The first involves thermal activation, promoting the flipping of individual magnetic domains or the motion of domain walls, leading to a monotonic temperature dependence of the coercive field[13,36]. The second concerns a temperature-induced reduction in l_z, which destroys coherent out-of-plane orbital motion and in-plane orbital magnetization. By contrast, the out-of-plane magnetic hysteresis vanishes above $T_{c\perp} \sim 4$ K (Extended Data Fig. 7c). This higher $T_{c\perp}$ probably originates from Stoner-type itinerant ferromagnetism associated with magnetic fluctuations[37], independent of l_z. The two distinct T_c values indicate that the in-plane and out-of-plane magnetization arise from different intrinsic mechanisms (Methods).

Discussion

Our observation of the giant in-plane orbital magnetization is unexpected. Although previous theoretical studies have explored potential mechanisms for realizing in-plane magnetization AHE/QAHE[18–20,38] in strongly spin–orbit-coupled materials, the experimental realization remains highly challenging. The emergence of in-plane magnetization AHE/QAHE requires not only the breaking of time-reversal symmetry through magnetization along an arbitrary direction but also other stringent symmetry conditions, such as breaking all reflection symmetries[18]. However, the intrinsic symmetry constraints inherent in most material systems have posed substantial barriers to achieving these effects in experimental settings. Some experimental studies have reported the observation of an in-plane Hall effect under zero $B_{\perp}$ in the antiferromagnetic heterodimensional VS_2–VS superlattice[39] and the magnetic Weyl semimetal $EuCd_2Sd_2$ (ref. 40). In these works,

it is noteworthy that the observations were made under a non-zero $B_{\parallel}$, and unfortunately, no anomalous Hall signal was detected for $B_{\parallel}$ and $B_{\perp} = 0$. Recent studies[41,42] reported R_{xx} hysteresis under in-plane fields but found no R_{xy} hysteresis or evidence of AHE. The R_{xx} hysteresis is ascribed to the extrinsic thermal origins[41], rather than intrinsic in-plane orbital magnetization and AHE. In graphene-based systems, achieving in-plane magnetic states with simultaneous breaking both time-reversal symmetry and all reflection symmetries is even more exceptionally challenging because of the high symmetry of the lattice structure and the negligibly weak SOC (about 40 μeV)[43,44].

To interpret TDAHE in rhombohedral graphene and to probe its microscopic origin, we perform systematic unrestricted Hartree–Fock calculations for nine-layer rhombohedral graphene (Supplementary Information). We find that as long as $D \gtrsim 0.3$ V nm^{-1}, the non-interacting Fermi surface of the system on slight electron doping $n \lessapprox 10^{12}$ cm^{-2} forms a ring-shape (Fig. 4d, top). Including the dominant long-range electron–electron Coulomb interactions would drive the system to a peculiar metallic state, which spontaneously breaks the time-reversal ($\mathcal{T}$), three-fold rotation (C_3) and vertical mirror ($\mathcal{M}_y$) symmetries of the system. This metallic phase is characterized by a crescent-shaped Fermi surface with full spin and valley polarization (Fig. 4d, middle). It possesses a notable in-plane orbital magnetization on the order of 2 μ_B per electron because of the breaking of $\mathcal{T}$, C_3 and $\mathcal{M}_y$ symmetries[45,46], and exhibits non-vanishing anomalous Hall conductivity due to the breaking of $\mathcal{T}$ symmetry. By virtue of non-vanishing in-plane orbital magnetization, this state naturally couples to an in-plane magnetic field, and its anomalous Hall conductivity flips sign with the reversal of in-plane field direction. We call such a state as transdimensional orbital ferromagnetic state[46]. When an electric field is small (or the n is large), the interacting ground state of electron-doped nine-layer rhombohedral graphene becomes a regular spin-valley polarized metal (Fig. 4d, bottom), which preserves C_3 symmetry, killing in-plane orbital magnetization.

Notably, the in-plane magnetization in our case is of pure orbital nature, the emergence of which is solely driven by electron–electron interactions without the need for SOC. When $\mathcal{T}$, C_3 and $\mathcal{M}_y$ symmetries are broken by a crescent-like Fermi surface, the system allows a finite in-plane orbital magnetization; in such a metallic ground state, electrons could, in principle, form an out-of-plane current loop to generate the in-plane orbital magnetization allowed by symmetry (Fig. 1a, right). By contrast, in all the previous theoretical proposals of AHE induced by in-plane magnetization, it is the spin magnetization that is within the 2D plane[18–20,38]; some specifically designed form of SOC is needed to convert the in-plane spin magnetization to out-of-plane orbital magnetization to generate AHE. Particularly, systems incorporating interfacial SOC are designed to reduce the symmetry of the system[47] for the AHE. In this sense, the TDAHE reported in this work is a genuine new class of AHE and is fundamentally different from the previous theoretical proposals of in-plane-magnetization induced AHE. This establishes a new model for correlation-driven topological phases beyond conventional AHE classifications. Moving forward, more exotic states such as integer- or fractional-quantized TDAHE states protected by topologically nontrivial Chern gaps can be realized by introducing tailored moiré potentials. These require future explorations of heterostructure and supercell engineering in the transdimensional regime. Complementary probes such as scanning SQUID-on-tip or nitrogen vacancy-centre magnetometry could show the nanoscale magnetic textures underlying TDAHE, providing deeper insight beyond transport measurements.

Online content

Any methods, additional references, Nature Portfolio reporting summaries, source data, extended data, supplementary information, acknowledgements, peer review information; details of author contributions and competing interests; and statements of data and code availability are available at https://doi.org/10.1038/s41586-026-10471-1.

1. Hall, E. On the possibility of transverse currents in ferromagnets. *Philos. Mag* **12**, 157–172 (1881).
2. Karplus, R. & Luttinger, J. M. Hall effect in ferromagnetics. *Phys. Rev.* **95**, 1154–1160 (1954).
3. Yao, Y. et al. First principles calculation of anomalous Hall conductivity in ferromagnetic bcc Fe. *Phys. Rev. Lett.* **92**, 037204 (2004).
4. Nagaosa, N., Sinova, J., Onoda, S., MacDonald, A. H. & Ong, N. P. Anomalous Hall effect. *Rev. Mod. Phys.* **82**, 1539–1592 (2010).
5. Hall, E. H. On a new action of the magnet on electric currents. *Am. J. Math.* **2**, 287–292 (1879).
6. Smit, J. The spontaneous Hall effect in ferromagnetics I. *Physica* **21**, 877–887 (1955).
7. Berger, L. Side-jump mechanism for the Hall effect of ferromagnets. *Phys. Rev. B* **2**, 4559–4566 (1970).
8. Jungwirth, T., Niu, Q. & MacDonald, A. H. Anomalous Hall effect in ferromagnetic semiconductors. *Phys. Rev. Lett.* **88**, 207208 (2002).
9. Burkov, A. A. Anomalous Hall effect in Weyl metals. *Phys. Rev. Lett.* **113**, 187202 (2014).
10. Ghimire, N. J. et al. Large anomalous Hall effect in the chiral-lattice antiferromagnet $CoNb_3S_6$. *Nat. Commun.* **9**, 3280 (2018).
11. Chang, C.-Z. et al. Experimental observation of the quantum anomalous Hall effect in a magnetic topological insulator. *Science* **340**, 167–170 (2013).
12. Liu, J. & Dai, X. Orbital magnetic states in moiré graphene systems. *Nat. Rev. Phys.* **3**, 367–382 (2021).
13. Sharpe, A. L. et al. Emergent ferromagnetism near three-quarters filling in twisted bilayer graphene. *Science* **365**, 605–608 (2019).
14. Serlin, M. et al. Intrinsic quantized anomalous Hall effect in a moiré heterostructure. *Science* **367**, 900–903 (2020).
15. Lu, Z. et al. Extended quantum anomalous Hall states in graphene/hBN moiré superlattices. *Nature* **637**, 1090–1095 (2025).
16. Park, H. et al. Observation of fractionally quantized anomalous Hall effect. *Nature* **622**, 74–79 (2023).
17. Li, T. et al. Quantum anomalous Hall effect from intertwined moiré bands. *Nature* **600**, 641–646 (2021).
18. Liu, X., Hsu, H.-C. & Liu, C.-X. In-plane magnetization-induced quantum anomalous Hall effect. *Phys. Rev. Lett.* **111**, 086802 (2013).
19. Ren, Y. et al. Quantum anomalous Hall effect in atomic crystal layers from in-plane magnetization. *Phys. Rev. B* **94**, 085411 (2016).
20. Liu, Z. et al. Intrinsic quantum anomalous Hall effect with in-plane magnetization: searching rule and material prediction. *Phys. Rev. Lett.* **121**, 246401 (2018).
21. Sha, Y. et al. Observation of a chern insulator in crystalline ABCA-tetralayer graphene with spin-orbit coupling. *Science* **384**, 414–419 (2024).
22. Han, T. et al. Large quantum anomalous Hall effect in spin-orbit proximitized rhombohedral graphene. *Science* **384**, 647–651 (2024).
23. Han, T. et al. Orbital multiferroicity in pentalayer rhombohedral graphene. *Nature* **623**, 41–47 (2023).
24. Lu, Z. et al. Fractional quantum anomalous Hall effect in multilayer graphene. *Nature* **626**, 759–764 (2024).
25. Shi, Y. et al. Electronic phase separation in multilayer rhombohedral graphite. *Nature* **584**, 210–214 (2020).
26. Liu, K. et al. Spontaneous broken-symmetry insulator and metals in tetralayer rhombohedral graphene. *Nat. Nanotechnol.* **19**, 188–195 (2024).
27. Han, T. et al. Correlated insulator and chern insulators in pentalayer rhombohedral-stacked graphene. *Nat. Nanotechnol.* **19**, 181–187 (2024).
28. Stoner, E. C. Collective electron ferromagnetism. *Proc. R. Soc. Lond. A Math. Phys. Sci.* **165**, 372–414 (1938).
29. Zhou, H. et al. Half-and quarter-metals in rhombohedral trilayer graphene. *Nature* **598**, 429–433 (2021).
30. Zhou, H. et al. Isospin magnetism and spin-polarized superconductivity in Bernal bilayer graphene. *Science* **375**, 774–778 (2022).
31. Huang, C. et al. Spin and orbital metallic magnetism in rhombohedral trilayer graphene. *Phys. Rev. B* **107**, L121405 (2023).
32. Wang, T., Vila, M., Zaletel, M. P. & Chatterjee, S. Electrical control of spin and valley in spin-orbit coupled graphene multilayers. *Phys. Rev. Lett.* **132**, 116504 (2024).
33. Polshyn, H. et al. Electrical switching of magnetic order in an orbital Chern insulator. *Nature* **588**, 66–70 (2020).
34. Choi, Y. et al. Superconductivity and quantized anomalous Hall effect in rhombohedral graphene. *Nature* **639**, 342–347 (2025).
35. Zhu, J., Su, J.-J. & MacDonald, A. H. Voltage-controlled magnetic reversal in orbital Chern insulators. *Phys. Rev. Lett.* **125**, 227702 (2020).
36. Emori, S., Umachi, C. K., Bono, D. C. & Beach, G. S. D. Generalized analysis of thermally activated domain-wall motion in Co/Pt multilayers. *J. Magn. Magn. Mater.* **378**, 98–106 (2015).
37. Park, H. et al. Observation of dissipationless fractional Chern insulator. *Nat. Phys.* **22**, 389–395 (2026).
38. Cao, J. et al. In-plane anomalous Hall effect in $\mathcal{PT}$-symmetric antiferromagnetic materials. *Phys. Rev. Lett.* **130**, 166702 (2023).
39. Zhou, J. et al. Heterodimensional superlattice with in-plane anomalous Hall effect. *Nature* **609**, 46–51 (2022).
40. Nakamura, A. et al. In-plane anomalous Hall effect associated with orbital magnetization: measurements of low-carrier density films of a magnetic Weyl semimetal. *Phys. Rev. Lett.* **133**, 236602 (2024).
41. Dutta, R., Ghosh, A., Watanabe, K., Taniguchi, T. & Das, A. Resistance hysteresis in twisted bilayer graphene: intrinsic versus extrinsic effects. Preprint at https://doi.org/10.48550/arXiv.2504.06380 (2025).
42. Mukherjee, A. et al. Superconducting magic-angle twisted trilayer graphene with competing magnetic order and moiré inhomogeneities. *Nat. Mater.* **24**, 1400–1406 (2025).
43. Arp, T. et al. Intervalley coherence and intrinsic spin–orbit coupling in rhombohedral trilayer graphene. *Nat. Phys.* **20**, 1413–1420 (2024).

44. Kane, C. L. & Mele, E. J. Quantum spin Hall effect in graphene. *Phys. Rev. Lett.* **95**, 226801 (2005).
45. Antebi, O., Stern, A. & Berg, E. In-plane orbital magnetization as a probe for symmetry breaking in strained twisted bilayer graphene. *Phys. Rev. B* **105**, 104423 (2022).
46. Li, M. et al. Fermi lune and transdimensional orbital magnetism in rhombohedral multilayer graphene. Preprint at https://doi.org/10.48550/arXiv.2505.05414 (2025).
47. Kao, I.-H. et al. Magnetization dependent in-plane anomalous Hall effect in a low-dimensional system. Preprint at https://doi.org/10.48550/arXiv.2505.06829 (2025).

Publisher's note Springer Nature remains neutral with regard to jurisdictional claims in published maps and institutional affiliations.

Springer Nature or its licensor (e.g. a society or other partner) holds exclusive rights to this article under a publishing agreement with the author(s) or other rightsholder(s); author self-archiving of the accepted manuscript version of this article is solely governed by the terms of such publishing agreement and applicable law.

© The Author(s), under exclusive licence to Springer Nature Limited 2026

Methods

Device fabrication

The rhombohedral graphene and hBN flakes are prepared by mechanical exfoliation of bulk crystals. The rhombohedral domains of ennealayer graphene flakes are detected by a confocal Raman system (WITec Alpha 300R) under a 532-nm excitation laser at room temperature (Extended Data Fig. 1a,b). The rhombohedral domains are subsequently isolated using an anodic-oxidation-assisted atomic force microscope cutting[48,49]. The van der Waals heterostructures are fabricated using our 'pick-up method'[50] to achieve a multilayer heterostructure with the ennealayer graphene encapsulated by two flakes of hexagonal boron nitride (hBN) and thin graphite flakes as the top and bottom gates. We determine that our nine-layer rhombohedral graphene device has a pure ABCABCABC stacking based on the analysis[25] similar to that of both the Raman 2D peak profile and the transport data under in-plane magnetic field (Extended Data Fig. 2e,f). Electron-beam lithography is used to write an etch mask to define the Hall-bar geometry and the electrodes. Redundant regions are etched away by CHF_3/O_2 plasma. Finally, the ennealayer graphene and gates are edge-contacted by e-beam evaporating thin metal layers consisting of Cr/Pd/Au (1 nm/15 nm/100 nm).

Layer rhombohedral (ABC-stacked) graphene is determined using three mutually consistent methods: calibrated optical-contrast analysis (Supplementary Fig. 3a), atomic force microscopy (AFM) thickness measurement (Supplementary Fig. 3b) and Landau-fan analysis (Supplementary Fig. 3c,d). Optical-contrast calibration is performed using reference regions of known layer numbers on the same wafer, yielding a contrast value ΔG consistent with that of a nine-layer graphene. To avoid systematic errors associated with AFM on SiO_2, the flake thickness is measured after full hBN encapsulation, giving a total thickness of about 3.0 nm, corresponding to nine layers based on the 0.334 nm interlayer spacing. Finally, Landau-fan measurements at $D = 0$ show the most robust Landau-level gap at filling factor $\nu_{LL} = -18$, confirming the nine-layer nature of the device. These three independent approaches provide consistent evidence for the nine-layer rhombohedral stacking configuration.

Measurements

The transport measurements are performed in two systems, a dilution fridge with a base temperature of 15 mK and a VTI fridge down to 1.5 K, both of which have superconducting magnets. All data are taken using the standard four-terminal configuration with lock-in amplifier techniques by sourcing an a.c. current I between 2 nA and 10 nA at a frequency of 17.777 Hz. All electrical contacts exhibit low and uniform resistance (about 1.5 kΩ per pin), ensuring negligible contact effects in transport measurements (Extended Data Fig. 1c). Measurements in Fig. 3b–e are performed in two separate cooldowns with slightly different base temperatures (15 mK and 20 mK, respectively). The hysteresis loops in our devices are reproducible under different sweep rates for both out-of-plane and in-plane magnetic fields, and field-induced heating is negligible (Supplementary Fig. 4). Top and bottom graphite gates with voltages V_T and V_B allow us to independently tune carrier density: $n = (C_B V_B + C_T V_T)/e$, and displacement field: $D = (C_B V_B - C_T V_T)/2$, where C_T is the top gate capacitance and C_B is the bottom gate capacitance. The data of longitudinal conductivity σ_{xx} and Hall conductivity σ_{xy} are obtained from the measured resistances by $\sigma_{xx} = \rho_{xx}/(\rho_{xx}^2 + R_{xy}^2)$. The data presented in the main text is based on devices A and B. We also report experimental data across devices with varying thicknesses, including 3-layer, 5-layer, 7-layer, two 9-layer, 10-layer, two 11-layer, and about 5 nm samples, and show that TDAHE in our ABC samples is robust for an intermediate thickness window (roughly corresponding to about 2–5 nm in our devices) and weak or absent for much thinner or much thicker samples (Extended Data Fig. 10).

We note that finite couplings between longitudinal and transverse directions would mix R_{xx} and R_{xy} signals. According to that R_{xy} is anti-symmetric with respect to the magnetic field B, whereas R_{xx} is symmetric, we can separate the two components using standard symmetrization and anti-symmetrization procedures during data processing. Similar to the out-of-plane magnetic field case, the symmetrization and anti-symmetrization procedures are also valid for in-plane magnetic fields in our system, which breaks time-reversal symmetry, mirror symmetry and C_3. In TDAHE regime, the in-plane magnetic field $B_\parallel$ induces a magnetization component M_y, which satisfies $M_y(B_\parallel) = -M_y(-B_\parallel)$, just as the out-of-plane magnetization $M_z(B_\perp) = -M_z(-B_\perp)$. Therefore, the anti-symmetrization procedure $R_{xy}^{\mathrm{anti}}(B_\parallel) = \frac{R_{xy}(B_\parallel) - R_{xy}(-B_\parallel)}{2}$ is valid and physically justified in our system. The symmetrization procedure for R_{xx} is as follows: $R_{xx}^{\mathrm{sym}}(B,\uparrow) = ((R_{xx}(B,\uparrow) + R_{xx}(-B,\downarrow))/2$ and $R_{xx}^{\mathrm{sym}}(B,\downarrow) = ((R_{xx}(B,\downarrow) + R_{xx}(-B,\uparrow))/2$. The anti-symmetrization procedure for R_{xy} is as follows: $R_{xy}^{\mathrm{antisym}}(B,\uparrow) = ((R_{xy}(B,\uparrow) - R_{xy}(-B,\downarrow))/2$, and $R_{xy}^{\mathrm{antisym}}(B,\downarrow) = ((R_{xy}(B,\downarrow) - R_{xy}(-B,\uparrow))/2$, where ↑ and ↓ indicate the direction of the magnetic field sweeping.

Alignment calibration and quantification of the residual tilt

To quantify any residual out-of-plane field component, we perform a nulling calibration procedure. The experiment is carried out in a vector magnet system equipped with three orthogonal field components (B_x, B_y and B_z). During sample loading, we carefully align the out-of-plane direction of the sample along the B_z axis. After sample loading, we focus on correcting any angular misalignment with an angle ψ between sample out-of-plane and B_z direction (Extended Data Fig. 5c). The calibration is carried out in a choosing region of the phase diagram (defined by n, D), in which only an out-of-plane hysteresis is present, with no in-plane hysteresis (quarter-metal regions in Fig. 2b). We intentionally choose this region because it provides a sensitive and unambiguous 'magnetic-field meter': the Hall response exhibits a clear B_z-driven hysteresis loop while remaining insensitive to purely in-plane fields, ensuring that any loop-centre shift can be attributed to a residual perpendicular component rather than an intrinsic in-plane hysteresis. Under eight different small positive and negative values of B_y, we sweep the perpendicular field B_z to obtain its hysteresis loop (Extended Data Fig. 5). For each fixed B_y, we sweep B_z through the full hysteretic range and recorded $R_{xy}(B_z)$, from which the coercive fields are extracted as the switching fields at which R_{xy} changes sign (or equivalently, the midpoint of the sharp transition), yielding H_{cup} and H_{cdown} for the up-sweep and down-sweep branches, respectively. Owing to the small tilt angle ψ (Extended Data Fig. 5c) between the sample out-of-plane and B_z direction, the applied in-plane field B_y introduces a component $B_{z0} = B_y \sin(\psi)$ along the sample out-of-plane direction, which causes a shift in the centre of the B_z hysteresis loop. We extract the coercive fields H_{cup} and H_{cdown} for each B_y, and determine the loop-centre shift as $B_{z0} = B_y \cdot \sin(\psi) = \frac{H_{\mathrm{cup}} + H_{\mathrm{cdown}}}{2}$. Here, the quantity $(H_{\mathrm{cup}} + H_{\mathrm{cdown}})/2$ directly measures the offset of the hysteresis-loop centre along the B_z axis, independent of the loop width. By fitting the relation between B_{z0} and B_y, the slope k gives $\sin(\psi)$, from which we obtain the offset angle $\psi = \arcsin(k) \approx -1.2°$ (Extended Data Fig. 5d). For the in-plane sweeps reported in the origin and revised manuscripts, we apply a compensating perpendicular field to null this residual component. Specifically, for each target in-plane field value B_y, we simultaneously apply a correction field $B_z^{\mathrm{comp}} = -B_y \sin(\psi)$ such that the net perpendicular component along the sample normal satisfies $B_z^{\mathrm{net}} \approx 0$ during the entire in-plane sweep. This compensation is implemented in the vector magnet control by co-sweeping B_z together with B_y according to the above linear relation. After applying this correction, the B_z-hysteresis-loop centre remains fixed at zero within experimental resolution, providing an internal validation that the residual out-of-plane component is effectively nulled. Using the same calibration and correction procedure, we also extract an offset angle of 1.78° along the B_x direction. The calibration and correction procedure is shown in Extended Data Fig. 5b,e.

Apart from carrying out the careful tilt angle compensation described above, we also provide direct evidence to clarify that the magnetic

hysteresis observed under out-of-plane field sweeps and that observed under in-plane field sweeps are not artefacts arising from field components induced by sample tilt, but instead originate from two independent, fundamentally distinct, intrinsic physical mechanisms. We have measured the temperature dependence of both the in-plane and out-of-plane AHE states (Extended Data Fig. 7c). The critical temperature T_c, at which the Hall hysteresis vanishes, reflects the characteristic energy scale of each state. The temperature dependence of the Hall hysteresis measured under out-of-plane field shows that the hysteresis disappears around $T_{c\perp} > 4$ K (Extended Data Fig. 7c). By contrast, the hysteresis observed under nominally in-plane field disappears at $T_{c\parallel} \approx 1.6$ K, substantially lower than $T_{c\perp}$. If the in-plane hysteresis are due to a small perpendicular component caused by sample tilt, we would expect the temperature scale to match that of the intrinsic out-of-plane magnetic order; this is not the case. This unambiguously demonstrates that the in-plane and out-of-plane AHE states originate from two independent, fundamentally distinct, intrinsic physical mechanisms.

Coherent-transport length scale l_z and thickness window for TDAHE

Microscopically, the effective l_z may be limited by more than one mechanism. In layered systems, the out-of-plane processes relevant to our phenomenon can be curtailed by vertical momentum-relaxing scattering, which sets a transport length scale (the mean free path), or by phase decoherence arising from inelastic processes, which sets a coherence length scale. Here, we estimate the out-of-plane mean free path in our rhombohedral graphene system.

We note that it is experimentally extremely challenging—if not practically impossible—to directly measure the out-of-plane mean free path and/or coherent length in our rhombohedral graphene system. Here l_z should be viewed as an effective out-of-plane coherence length scale that bounds the vertical extent over which coherent interlayer orbital motion remains coherent, and as an operational, experimentally bounded vertical length scale controlling the persistence of the transdimensional response in our devices its magnitude is consistent (to order of magnitude) with a Drude-based estimate from transport. To precisely determine the mean free path in graphite, we need to measure the cross-plane electrical conductivity ($\sigma_\perp$), from which the relaxation time and, consequently, the mean free path along the out-of-plane direction can be extracted. This difficulty originates from both device geometry and electrostatic design constraints: our samples are dual-gated Hall-bar devices, in which the top and bottom gates are required to independently tune the displacement field (D) and carrier density (n). Because the observed TDAHE phase appears only at large D and low n (Fig. 3a, green region), both top and bottom gates must be simultaneously active. However, to measure the out-of-plane conductivity, we would need to place electrodes on both the top and bottom surfaces of the rhombohedral graphene, which would inevitably screen the dual gates and prevent tuning D and n into the TDAHE regime. This device geometry thus leaves no practical way to introduce additional vertical contacts or electrodes without disturbing the uniformity of the displacement field, making any direct measurement of $\sigma_\perp$ unfeasible at TDAHE regime. Given these experimental limitations, we estimate the mean free path indirectly by combining known bulk graphite transport data with theoretical parameters of rhombohedral graphene.

From transport measurements of bulk graphite, the ratio between vertical and in-plane conductivities is found to be approximately 10^{-4} (ref. 51). Applying this ratio to rhombohedral graphene in the transdimensional regime, we can estimate the out-of-plane conductivity as $\sigma_\perp \approx 10^{-4}\sigma_\parallel \approx 10^{-6}\ \Omega^{-1}$, given that the measured in-plane conductivity is about $\sigma_\parallel \approx 10^{-2}\ \Omega^{-1}$ (corresponding to a resistance of roughly 100 Ω when the sample is not in the insulating state at zero magnetic field). When the carrier density is $n \approx 10^{12}\ \mathrm{cm}^{-2}$, the relaxation time along the vertical direction, $\tau_\perp$, can be estimated using the Drude formula: $\sigma_\perp = \frac{e^2 n \tau_\perp}{m_\perp^*}$, where $m_\perp^* \approx 5m_0$ is the out-of-plane effective mass of rhombohedral graphene (m_0 is the electron mass)[46] and e is the elementary charge. From these parameters, we obtain $\tau_\perp \sim 10^{-14}$ s. The out-of-plane Fermi velocity of rhombohedral graphene, $v_\perp$, is typically about one order of magnitude smaller than the in-plane Fermi velocity of graphene, that is, $v_\perp \sim 10^5\ \mathrm{m\ s}^{-1}$ (ref. 46). Consequently, the out-of-plane mean free path can be estimated as $v_\perp \tau_\perp \approx 2$ nm. We note that this is only a qualitative estimate, and the actual value of mean free path may vary depending on specific sample conditions, but it should generally be on the order of a few nanometres. Furthermore, our calculations (Supplementary Information section 4) suggest that the in-plane magnetic state with magnetization pointing in crystalline y-direction exhibits an in-plane current flowing in the x-direction, eventually forming a current loop in the x–z plane. Most importantly, the in-plane current density is localized within a few layers that are closest to the surface layer (about 7–8 layers), which is of the order of magnitude as the estimated mean free path.

To validate the generality of our hypothesis, we have fabricated and measured multiple rhombohedral graphene devices with different thicknesses, including three-layer, five-layer, seven-layer, two nine-layer, 10-layer, two 11-layer, and about 5 nm samples, as summarized in Extended Data Fig. 8. The main experimental findings are as follows: (1) robust TDAHE is observed in devices with layer numbers in the intermediate range (2–5 nm range) for seven-layer, two independent nine-layer devices, 10-layer, two 11-layer and 5 nm devices; (2) no TDAHE is observed in the very thin devices we measured (three-layer and five-layer samples), which is consist with previous reports. This indicates a lower thickness bound below which the transdimensional mechanism does not develop; and (3) in a relatively thick rhombohedral graphene device (thickness about 5 nm), we observe only a very weak in-plane hysteresis (very small TDAHE), suggesting that this thickness marks the upper bound beyond which coherent out-of-plane orbital motion becomes suppressed. Taken together, these device-by-device measurements indicate that TDAHE in our rhombohedral graphene samples is robust for an intermediate thickness window (roughly corresponding to about 2–5 nm in our devices) and weak or absent for much thinner or much thicker samples. This thickness range of TDAHE in our multilayer rhombohedral graphene devices is consistent with our estimated l_z. We note that this is only a rough estimate. At the same time, measurements across multiple devices spanning thicknesses from 3 to 15 layers experimentally identify the transdimensional regime, for which l_z serves as a conceptual, phenomenological and operational vertical length scale.

Last, we should claim that in transdimensional regime, the current along out-of-plane direction is viewed as coherent interlayer tunnelling current between layers within a finite thickness, rather than transport of 3D or quasi-3D Bloch electrons. Therefore, a Bloch-type out-of-plane band structure is not a prerequisite for having a finite interlayer tunnelling current.

In-plane magnetization orientation and field-angle dependence

The orientation of the crescent-shaped Fermi contour in the TDAHE state is defined with respect to the crystallographic axes. In the spontaneously symmetry-broken TDAHE phase, the order parameter is pinned to one of three crystallographically equivalent in-plane directions related by the lattice C_3 symmetry, giving rise to three domain orientations (α, β, γ), each with two time-reversed partners (more details in our theoretical paper[46]). Consequently, the in-plane orbital magnetization $\mathbf{M}_\parallel$ can point along three symmetry-related crystalline directions, and the observed Hall response depends on which domain is realized.

Experimentally, the relevant control parameter is the projection of the applied in-plane magnetic field $\mathbf{B}_\parallel$ onto the domain magnetization direction, through the Zeeman coupling $-\mathbf{M}\cdot\mathbf{B}$. Domain selection and switching under $\mathbf{B}_\parallel$ are, therefore, governed by $\mathbf{B}_\parallel \cdot \mathbf{M}_\parallel$: when $\mathbf{B}_\parallel$ is aligned closer to $\mathbf{M}_\parallel$ of a given domain, the energy bias is larger and switching occurs at a smaller coercive field, whereas a larger coercive field is required when $\mathbf{B}_\parallel$ is closer to orthogonal to $\mathbf{M}_\parallel$.

To directly determine how the broken-symmetry orientation is set in our system, we perform angle-dependent measurements of the in-plane-field hysteresis. We define the in-plane field angle θ relative to the direction at which the coercive field is minimal ($\theta = 0°$), and extract the coercive field $H_c(\theta)$ from hysteresis loops measured at each θ (Extended Data Fig. 10a,c). The resulting $H_c(\theta)$ exhibits an approximately threefold angular dependence, consistent with three crystallographically equivalent domain orientations (α, β, γ) related by C_3 symmetry. Furthermore, the hysteresis polarity reverses across $\theta \approx 30°$ and $\theta \approx 150°$ (Extended Data Fig. 10a), indicating domain conversion between symmetry-related TDAHE domains. Near these transition angles, the coercive field is not well-defined because of the conversion process and is therefore not reported. In an ideal C_3-symmetric case, we would expect an additional sharp polarity reversal near $\theta \approx 90°$, corresponding to a crossover between the β and γ domains. In our device, we instead observe a continuous hysteresis polarity across $\theta \approx 90°$, suggesting weak explicit symmetry breaking (for example, residual uniaxial strain or disorder) that lifts the near-degeneracy between the β and γ domains and stabilizes one domain over an extended angular range (Extended Data Fig. 10c). Nevertheless, the robust threefold trend in $H_c(\theta)$, together with the observed polarity reversals, provides direct evidence that the TDAHE state supports multiple symmetry-related domains whose orientations are tied to the crystal axes.

Symmetry analysis of the in-plane magnetic state

For the in-plane magnetic state showing TDAHE, the in-plane orbital magnetization $M_\parallel$ is closely related to the crystallographic symmetries. Specifically, the time-reversal operation $\mathcal{T}$ reverses the magnetization: $\mathcal{T} M_\parallel \mathcal{T}^{-1} = -M_\parallel$, so the presence of $\mathcal{T}$ symmetry enforces $M_\parallel$ equal to zero. Similarly, the C_3 rotation operation symmetrically rotates $M_\parallel$ about the z axis: $C_3 M_\parallel C_3^{-1} = R(2\pi/3) M_\parallel$, where $R(2\pi/3)$ is the rotation matrix about the z axis by an angle $2\pi/3$. The presence of C_3 symmetry also enforces $M_\parallel = 0$. The vertical mirror operation $\mathcal{M}_y$ preserves the component of the in-plane orbital magnetization along the x-direction, and reverses the magnetization along the y-direction, $\mathcal{M}_y M_\parallel \mathcal{M}_y^{-1} = (M_{\parallel,x}, -M_{\parallel,y})$. Therefore, the presence of $\mathcal{M}_y$ symmetry enforces the y component of in-plane magnetization vanishing.

Therefore, any two of these symmetries (such as $\mathcal{M}_y$ and C_3, C_3 and $\mathcal{T}$, or $\mathcal{M}_y$ and $\mathcal{T}$) will protect $M_\parallel = 0$; or, in other words, the presence of either C_3 or $\mathcal{T}$ symmetry would enforce the magnetization to be vanishing. However, when all three symmetries are broken, the system allows a finite in-plane magnetization, particularly along the crystalline y-direction, which is the phenomenon observed in our work.

Symmetry origin of the transverse anomalous Hall response

In our theory, the metallic ground state with peculiar crescent-shaped Fermi surface exhibits both in-plane and out-of-plane magnetizations. The out-of-plane magnetization is allowed because this peculiar metallic state spontaneously breaks time-reversal, rotational and mirror symmetries. The out-of-plane magnetization generates Berry curvature, which leads to the appearance of AHE. When an in-plane magnetic field is applied, the reversal of in-plane field direction would flip the in-plane magnetization; and as the in-plane magnetization is coupled with the out-of-plane component, the reversal of in-plane magnetization is accompanied by the flip of the out-of-plane magnetization, which changes the sign of anomalous Hall conductance[46].

To elaborate, the in-plane magnetization is switched by an in-plane magnetic field, and this switching induces a change in the out-of-plane magnetization. The resulting change in out-of-plane magnetization alters the Berry curvature, flipping its sign. This flip in Berry curvature affects the Hall response and leads to the TDAHE reported in this work. This mechanism provides an explanation for why a transverse-field AHE can emerge even when the current and magnetization are not rigorously perpendicular to each other.

Data availability

The data that support the findings of this study are available from the corresponding authors upon request.

48. Masubuchi, S., Ono, M., Yoshida, K., Hirakawa, K. & Machida, T. Fabrication of graphene nanoribbon by local anodic oxidation lithography using atomic force microscope. *Appl. Phys. Lett.* **94**, 082107 (2009).
49. Li, H. et al. Electrode-free anodic oxidation nanolithography of low-dimensional materials. *Nano Lett.* **18**, 8011–8015 (2018).
50. Wang, L. et al. One-dimensional electrical contact to a two-dimensional material. *Science* **342**, 614–617 (2013).
51. Dutta, A. K. Electrical conductivity of single crystals of graphite. *Phys. Rev.* **90**, 187–192 (1953).

Acknowledgements L.W. acknowledges support from the National Key Projects for Research and Development of China (grant nos. 2021YFA1400400 and 2022YFA1204700), the National Natural Science Foundation of China (grant nos. 12525403 and 12550404), the Natural Science Foundation of Jiangsu Province (grant nos. BK20253027 and BK20233001) and the HFNL Self-Deployed Project (ZB2025020200). G.Y. acknowledges a grant from the National Key R&D Program of China (no. 2024YFB3715405) and support from International Joint Lab of 2D Materials at Nanjing University and the Wuxi Feynman group. K.W. and T.T. acknowledge support from the JSPS KAKENHI (grant nos. 21H05233 and 23H02052) and the World Premier International Research Center Initiative (WPI), MEXT, Japan. J.L. acknowledges support from the National Key Research and Development Program of China (grant no. 2024YFA1410400) and the National Natural Science Foundation of China (grant no. 12174257). Y.Z. acknowledges support from the National Key R&D Program of China (grant no. 2022YFA1403700), NSFC 11674150 and the University Innovative Team in Guangdong Province 2020KCXTD001. The work of other authors was supported by the Synergetic Extreme Condition User Facility (https://cstr.cn/31123.02.SECUF).

Author contributions L.W. conceived and supervised the experiment. Q.L., Y.X. and J. Song fabricated the samples. Q.L., H.F. and Y.Z. performed the transport measurements with the help from A.W., J. Shen, J.-J.C., Z.T., K.S.N. and G.Y.; Q.L., L.W. Y.Z., H.J., X.-C.X., J.C.H., C.R.D. and J.L. analysed the data. M.L. and J.L. conducted theoretical calculations. K.W. and T.T supplied the hBN crystals. Q.L., J.L. and L.W. wrote the manuscript with input from all co-authors.

Competing interests The authors declare no competing interests.

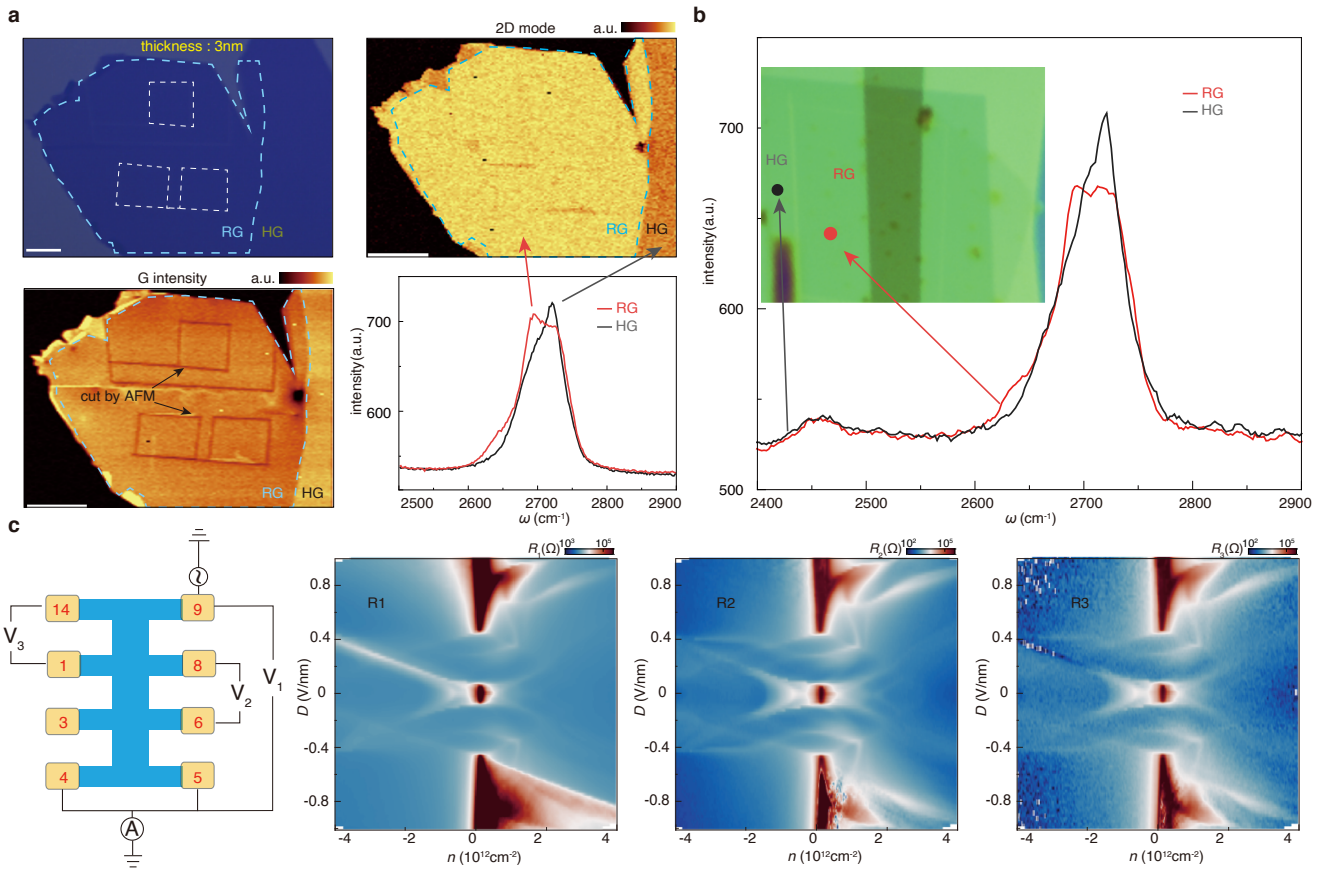
Additional information

Supplementary information The online version contains supplementary material available at https://doi.org/10.1038/s41586-026-10471-1.

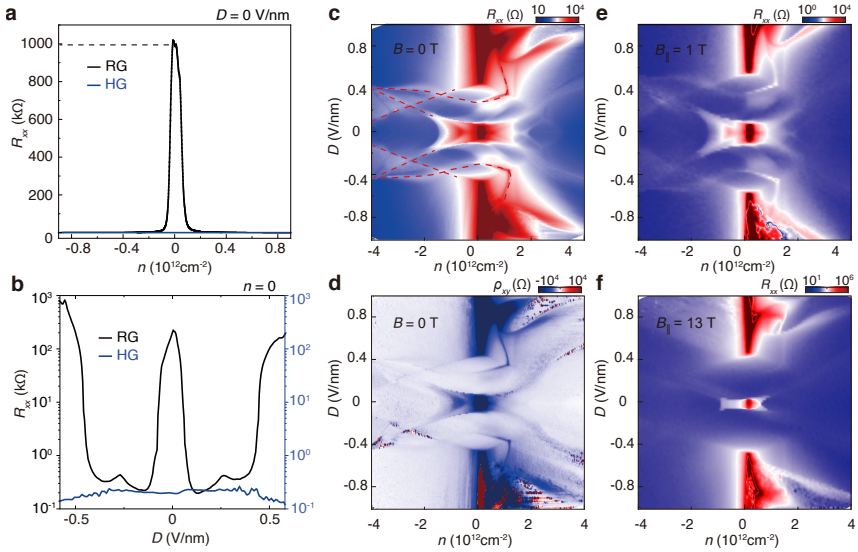
Correspondence and requests for materials should be addressed to Geliang Yu, Yue Zhao, Jianpeng Liu or Lei Wang.

Peer review information *Nature* thanks Manabendra Kuiri, Taige Wang and the other, anonymous, reviewer(s) for their contribution to the peer review of this work. Peer reviewer reports are available.

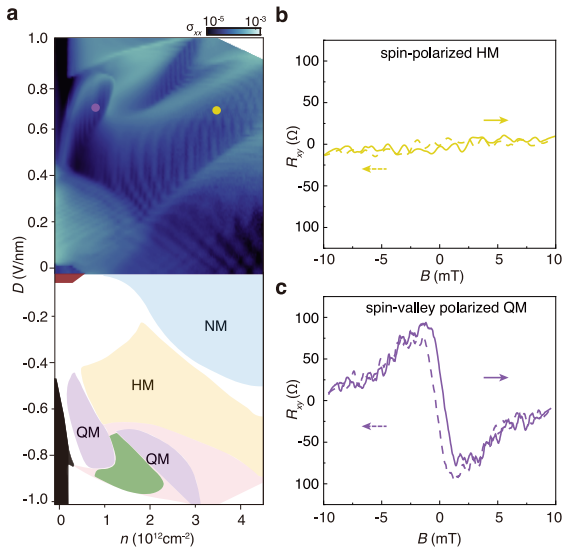
Reprints and permissions information is available at http://www.nature.com/reprints.



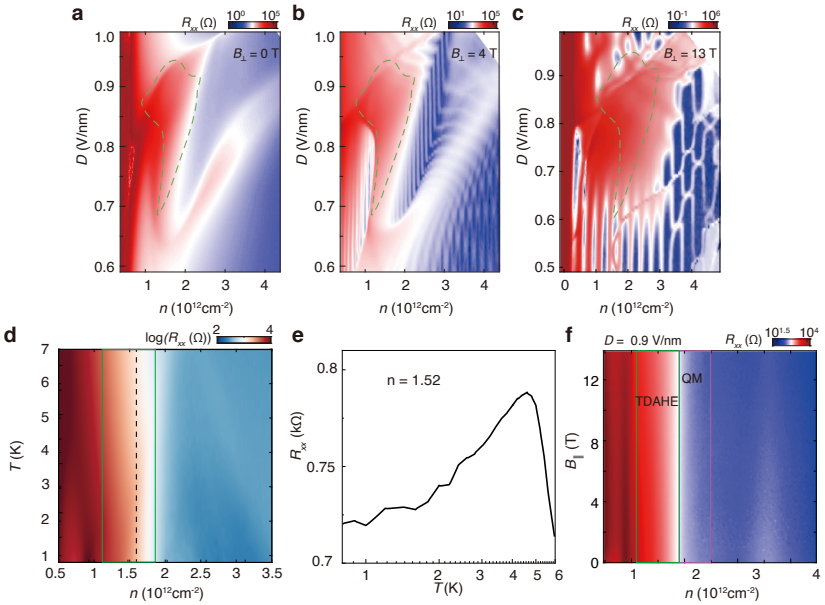
Extended Data Fig. 1 | Multi-stage verification of ABC stacking and uniform transport measurements. a, *Top left:* Optical image of an exfoliated 3-nm-thick, 9-layer graphene flake on a SiO_2/Si substrate, taken with a standard optical microscope. The cyan dashed line marks the boundary of the rhombohedral-stacked (RG, ABCABC…) region, which is isolated by anodic-oxidation-assisted AFM cutting (white dashed lines). Scale bar: 10 μm. *Top right:* Raman mapping of the 2D-mode peak position for the same flake. The darker domain corresponds to hexagonal stacking (HG, ABABAB…), while the brighter region, enclosed by the cyan dashed line, indicates rhombohedral stacking. *Bottom left:* Raman mapping of the integrated G-band intensity, where the darker region represents rhombohedral stacking and the brighter region indicates hexagonal stacking. Scale bar: 10 μm. *Bottom right:* Representative Raman spectra of HG and RG regions in the 9-layer graphene, centered on the 2D mode. **b**, Raman spectra of the completed heterostructure device, showing consistent ABC stacking by comparing point spectra between the reference ABC and ABA regions. **c**, Longitudinal resistance R_{xx} measured at $B = 0$ T for all contact pairs across the device, confirming uniform transport behavior.



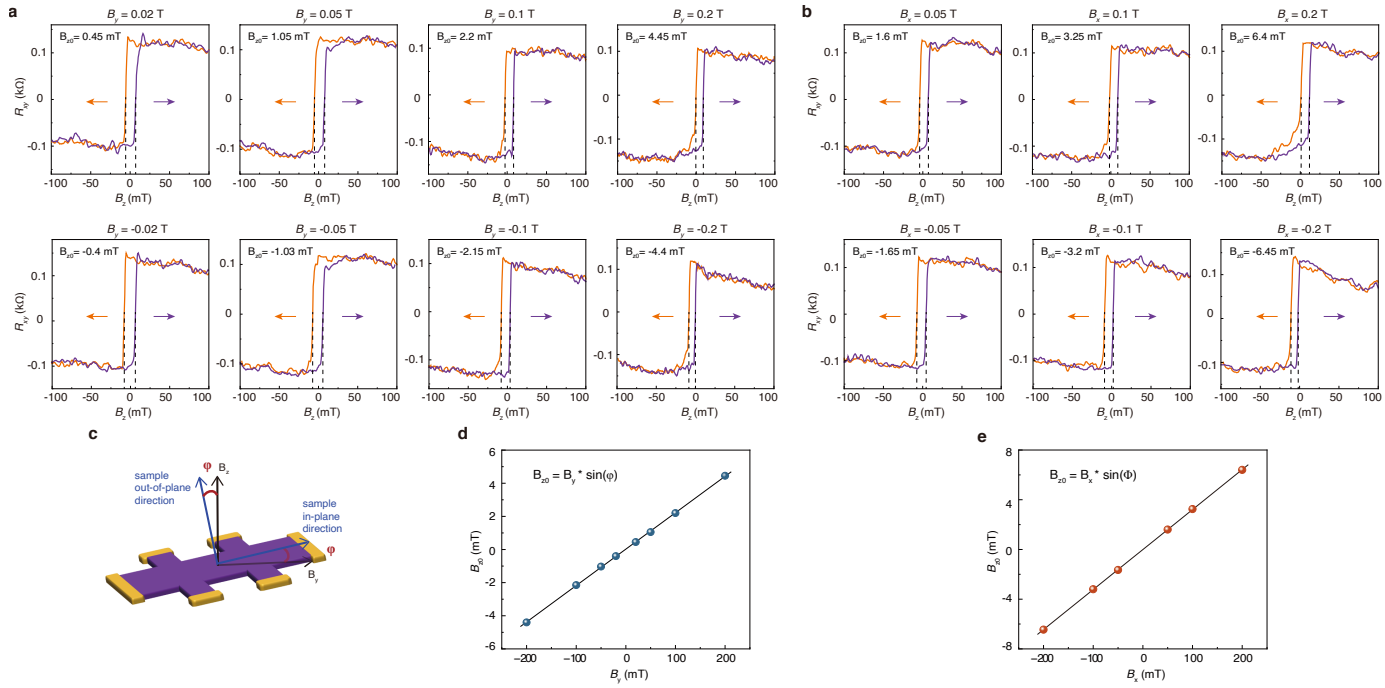
Extended Data Fig. 2 | phase diagram of 9-layer RG in different out-of-plane magnetic fields. a, Longitudinal resistance R_{xx} as a function of n at $D = 0$ V/nm, $T = 20$ mK, $B = 0$ T, with RG (black curve) and HG (blue curve) crystal structures. The black dashed line marks the resistance of 1000 kΩ. **b**, R_{xx} as a function of D at $n = 0$, $T = 20$ mK, $B = 0$ T, with RG (black curve) and HG (blue curve) crystal structures. **c**,**d**, Map of longitudinal resistance R_{xx} and Hall resistivity ρ_{xy} as functions of n and D at $T = 20$ mK, $B = 0$ T. The red dashed lines denotes several cross-like features occurring with increasing resistance, which may be associated with van Hove singularities. **e**,**f**, Map of longitudinal resistance R_{xx} under different in-plane magnetic fields: $B_{\parallel} = 1$ T and 13 T, as functions of n and D at $T = 20$ mK.



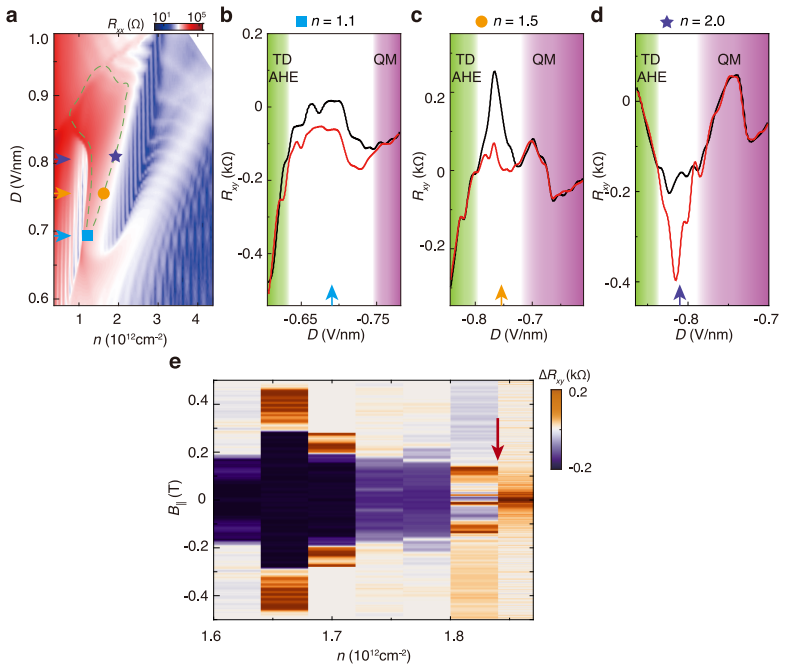
Extended Data Fig. 3 | Stoner ferromagnetism in QM region. a, Longitudinal conductivity σ_{xx} plotted versus n and the displacement field D for 0 V/nm ⩽ D ⩽ 1.0 V/nm, $B_\perp$ = 4 T, and the corresponding schematic diagram for different symmetry-broken phases. **b**,**c**, R_{xy} measured as $B_\perp$ is swept back and forth (marked by dashed and solid arrows) at yellow (**b**) and purple (**c**) points marked in **a**.



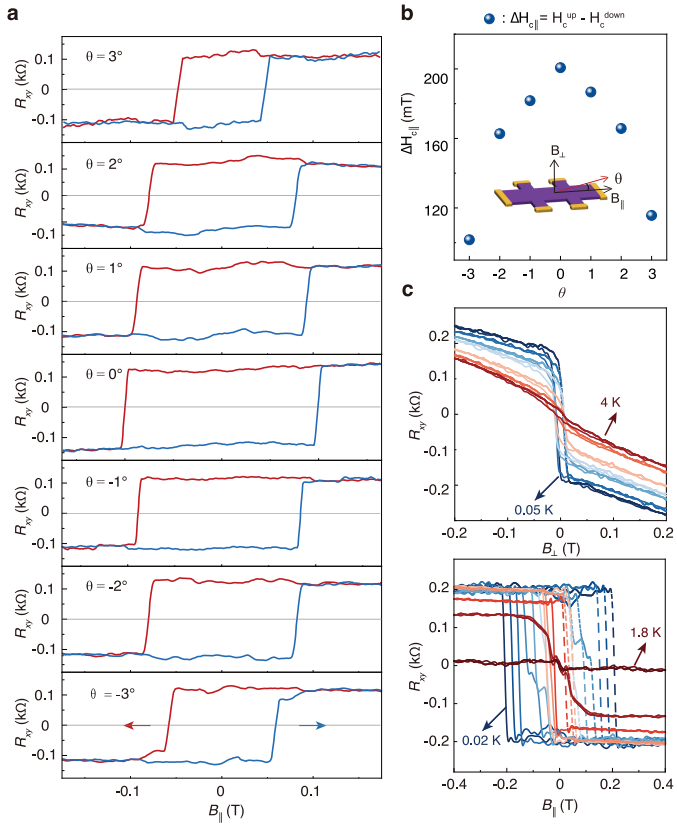
Extended Data Fig. 4 | Dependence of the R_{xx} on out-of-plane and in-plane magnetic fields, as well as temperature, in the TDAHE region. a–**c**, R_{xx} plotted versus n and D for 0.6 V/nm ⩽ D ⩽ 1.0 V/nm, at B = 0 T (**a**), $B_\perp$ = 4 T (**b**), $B_\perp$ = 13 T (**c**). The green dashed line in each figure denotes the boundary of TDAHE region. **d**, R_{xx} as a function of n and T at D = 0.9 V/nm. **e**, Line-cut of R_{xx} along T axis at $n = 1.52 \times 10^{12}$ cm^{-2}, which showing a metical behaviour. **f**, R_{xx} as a function of in-plane magnetic field $B_\parallel$ and doping n at D = 0.9 V/nm. The TDAHE region is between green lines, while quarter-metal (QM) region is between purple lines.



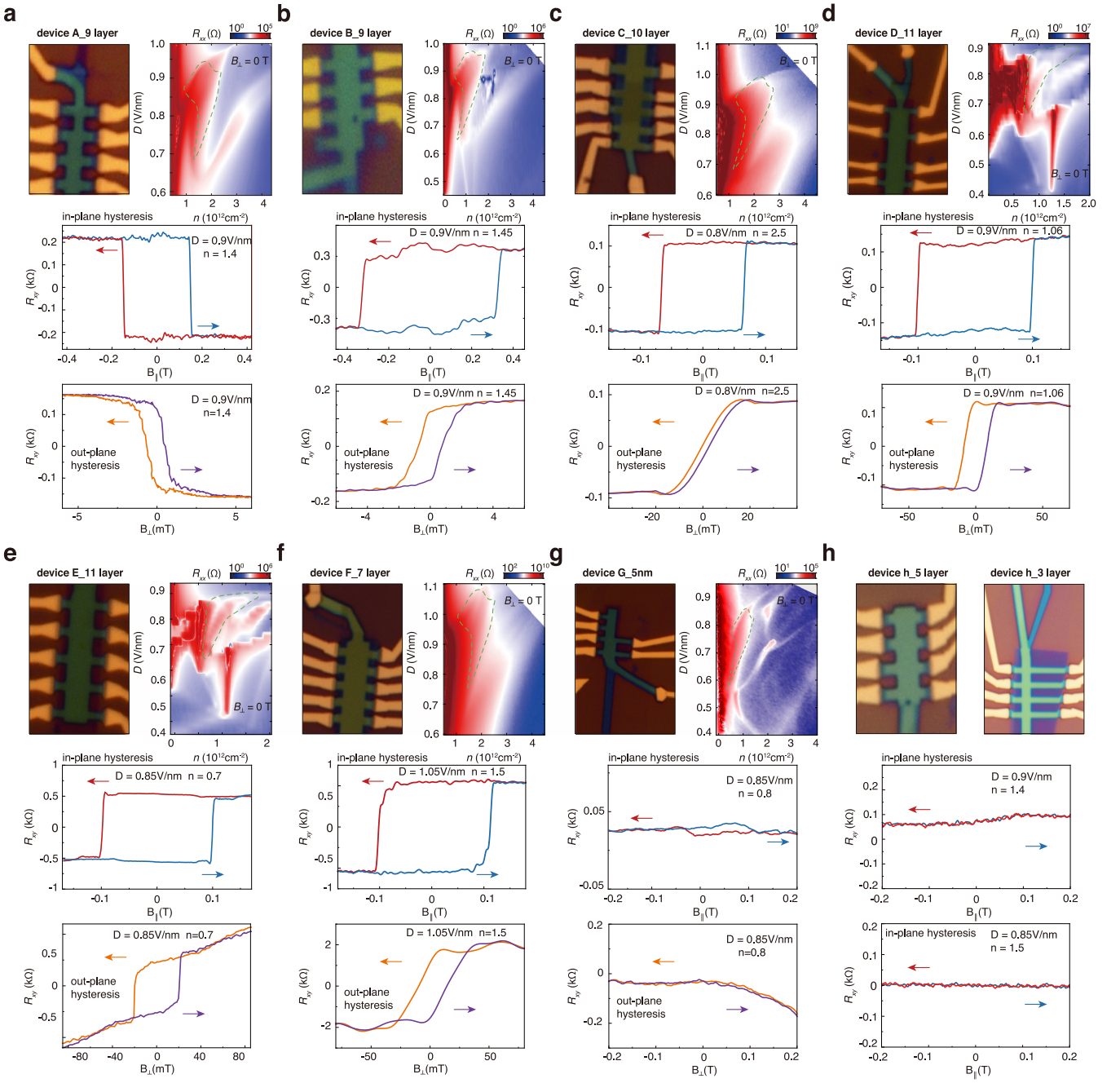
Extended Data Fig. 5 | Nulling calibration procedure and quantification of residual tilt. a, The illustration of the calibration procedure for correcting misalignment along the B_y axis. **b**, Similar calibration scheme applied along the B_x axis. **c**, Schematic of tilt angle φ between the sample out-of-plane and B_z direction. **d**,**e**, Extracted loop center B_{z0} as a function of By and B_x. The linear fit gives a slope corresponding to sin(φ) and sin(Φ), from which the tilt angle is determined to be 1.2° (B_y direction) and 1.78° (B_x direction).



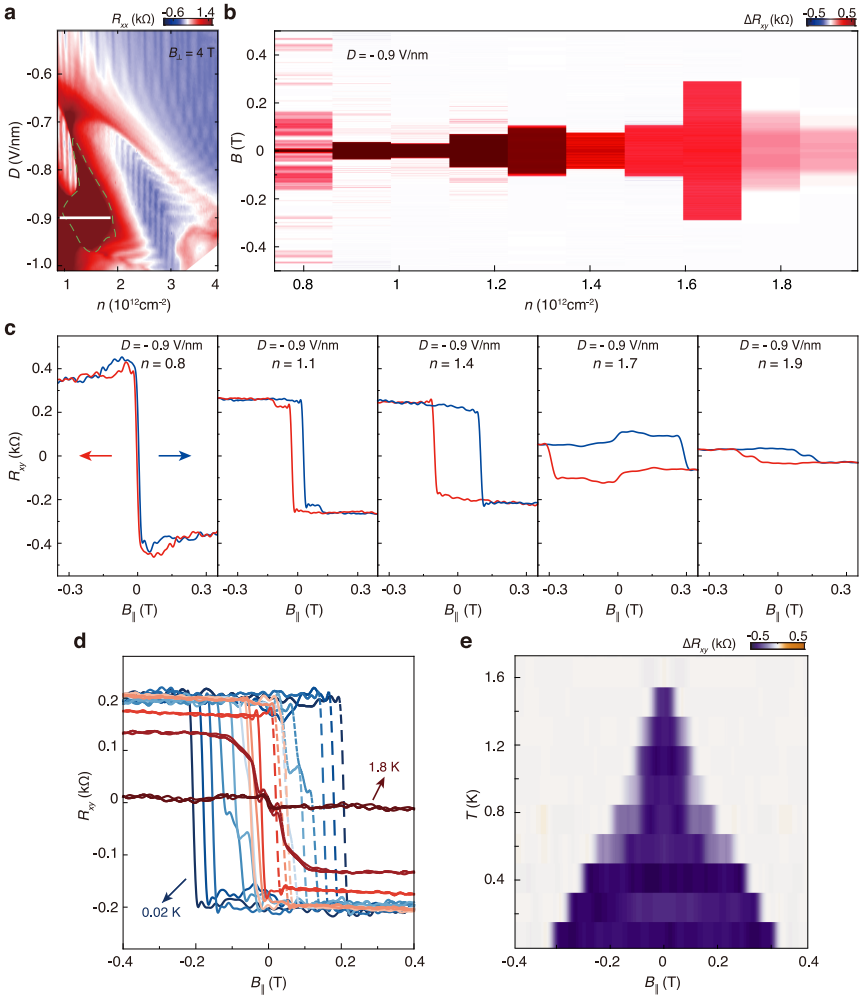
Extended Data Fig. 6 | Electrical hysteresis near the boundary of TDAHE and QM and Electrical switching of the magnetic order effect. a, R_{xx} plotted versus n and D, at $B_\perp = 4$ T. The green dashed line denotes the boundary of TDAHE region. **b**–**d**, Hall resistance R_{xy} measured as a function of D across the boundary between the QM and TDAHE phases, at the locations marked by the blue square (**b**), orange sphere (**c**), and purple pentagon (**d**) in **a**. The transition is strongly first order, showing hysteresis as a function of applied gate voltages. **e**, Hall resistance difference ΔR_{xy} as a function of n and $B_\parallel$ at $D = 0.9$ V/nm, for $1.6 \times 10^{12}\ \mathrm{cm}^{-2} \leqslant n \leqslant 1.9 \times 10^{12}\ \mathrm{cm}^{-2}$. The switching magnetic order behavior occurs near the density where the hystereses loop almost vanishes (marked by the red arrow).



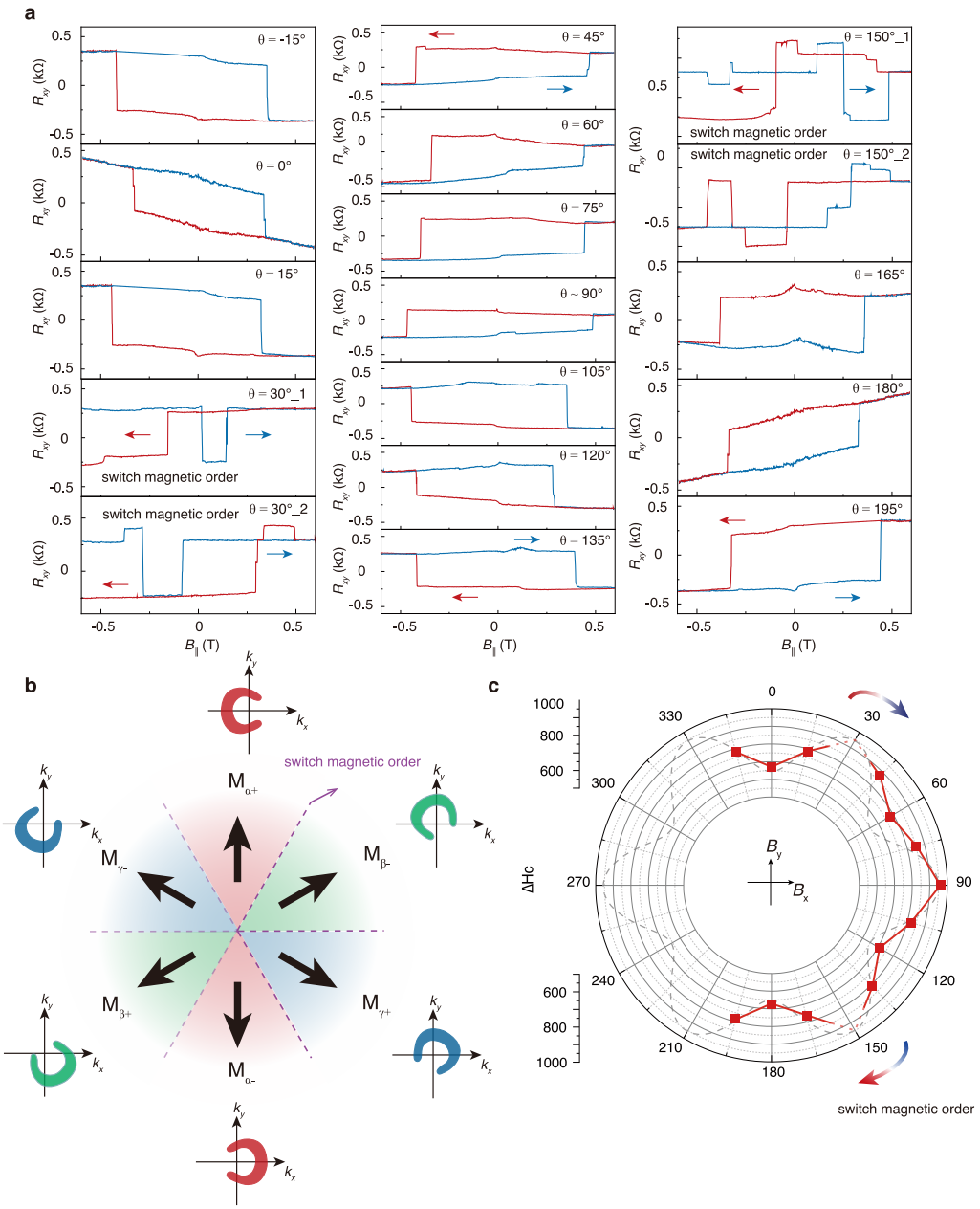
Extended Data Fig. 7 | Angle-dependent in-plane hysteresis and distinct temperature scales of out-of-plane and in-plane magnetic hysteresis. **a**, Measured hysteresis loops along several directions with tilt angles of ± 3°, ± 2°, ± 1°, and ± 0. 5° relative to the sample in-plane direction. Note that the $B_\parallel$ axis now is the real sample in-plane-direction magnetic field (defined as 0°), because it is after the nulling calibration procedure mentioned (Methods and Extended Data Fig. 6). **b**, Extracted in-plane coercive field $H_{c\parallel}$ as a function of tilt angle, showing a maximum at $\theta = 0°$ and monotonic decrease with increasing tilt. The inset shows the schematic of vector field orientation in the $B_\perp - B_\parallel$ plane, illustrating the applied tilt angles relative to the $B_\parallel$ axis. **c**, Temperature dependence of out-of-plane and in-plane magnetic hysteresis in device A. The out-of-plane hysteresis disappears around $T_c^\perp > 4\ K$, by contrast, the hysteresis observed under nominally in-plane field disappears at $T_c^\parallel \approx 1.6$ K.



Extended Data Fig. 8 | All nine rhombohedral graphene (RG) devices measured with seven exhibiting TDAHE with different sample thicknesses– a 7-layer RG, a 10-layer RG, two 9-layer RGs, two 11-layer RGs, and a 5 nm RG .



Extended Data Fig. 9 | In-plane orbital ferromagnetism at $D = -0.9$ V/nm and temperature dependence of in-plane magnetic hysteresis in Device A. a, R_{xx} plotted versus n and D for negative D at $B_\perp = 4$ T. **b**, Hall resistance difference ΔR_{xy} as a function of n and $B_\parallel$ at $D = -0.9$ V/nm, along the white line denoted in **a**. **c**, The magnetic-field-dependent R_{xy} at selected carrier density $n = 0.8, 1.1, 1.4, 17, 1.9$ (in units of 10^{12} cm^{-2}) at $D = -0.9$ V/nm, $T = 20$ mK. **d**,**e**, Temperature dependence of in-plane magnetic hysteresis in Device A.



Extended Data Fig. 10 | Evolution of the hysteresis loops under different in-plane field angles and threefold symmetry of H_c. **a**, Representative R_{xy} hysteresis loops measured at selected in-plane field angles θ, defined relative to the angle of minimal H_c (taken as $\theta = 0°$). Polarity reversals occur near $\theta \approx 30°$ and 150°, indicating switching between symmetry-related TDAHE domains; H_c is not extracted near these conversion angles. **b**, Illustration of the six symmetry-related domains $\alpha^{\pm}$, $\beta^{\pm}$, and $\gamma^{\pm}$. **c**, Polar plot of the extracted coercive field $H_c(\theta)$ (radial coordinate R), showing an approximately threefold angular dependence consistent with C_3-related domain orientations. The absence of a sharp reversal near $\theta \approx 90°$ suggests weak explicit symmetry breaking (e.g., residual strain or disorder).